Solar Cell Degradation Due to Proton Belt Enhancements During Electric Orbit Raising to GEO

Alexander R. Lozinski[1,2] (ID), **Richard B. Horne**[1] (ID), **Sarah A. Glauert**[1] (ID), **Giulio Del Zanna**[2] (ID), **Daniel Heynderickx**[3] (ID), and **Hugh D. R. Evans**[4] (ID)

[1]British Antarctic Survey, Cambridge, UK, [2]Department of Applied Mathematics and Theoretical Physics, University of Cambridge, Cambridge, UK, [3]DH Consultancy BVBA, Leuven, Belgium, [4]European Space Agency/European Space Research and Technology Centre, Noordwijk, Netherlands

Abstract The recent introduction of all-electric propulsion on geosynchronous satellites enables lower-cost access to space by replacing chemical propellant. However, the time period required to initially raise the satellite to geostationary orbit (GEO) is around 200 days. During this time the satellite can be exposed to dynamic increases in trapped flux, which are challenging to model. To understand the potential penalty of this new technique in terms of radiation exposure, the influence of several key parameters on solar cell degradation during the electric orbit raising period has been investigated. This is achieved by calculating the accumulation of nonionizing dose through time for a range of approaches. We demonstrate the changes in degradation caused by launching during a long-lived (hundreds of days) enhancement in megaelectron volt trapped proton flux for three different electric orbit raising scenarios and three different thicknesses of coverglass. Results show that launching in an active environment can increase solar cell degradation due to trapped protons by ~5% before start of service compared with a quiet environment. The crucial energy range for such enhancements in proton flux is 3–10 MeV (depending on shielding). Further changes of a few percent can occur between different trajectories, or when a 50-μm change in coverglass thickness is applied.

1. Introduction

The proton belt is a region of magnetically trapped protons at energies ranging from sub–megaelectron volt to hundreds of megaelectron volts. The radial profile of flux is energy dependent, extending from just outside Earth up to $L \sim 3.5$ at tens of megaelectron volts, with higher energies occupying a narrower range. Early work following its discovery established radial diffusion as a key mechanism for transporting trapped particles into the inner magnetosphere (Fälthammar, 1965; Parker, 1960; Tverskoy, 1965); this process redistributes the $\gtrsim$1-MeV proton belt at $L \gtrsim 1.25$. Fluxes at lower L and $\gtrsim$50-MeV energy are produced by the cosmic ray albedo neutron decay process (Jentsch, 1981; Selesnick et al., 2014), while the injection of solar energetic particles (SEPs) provides an external source of $\gtrsim$1-MeV protons at $L > 2$, with the solar origin confirmed by measurements of heavy ions (Mazur et al., 2013). The stable inner belt ($L \sim 1.5$) is formed over timescales of centuries (Selesnick et al., 2007), with observations indicating variability on approximately decade timescales (Selesnick et al., 2016). In the intermediate region ($L \sim 2$), variation in megaelectron volt flux occurs on approximately year timescales (Albert & Ginet, 1998; Spjeldvik, 2000), while the outer region ($L \gtrsim 2$) can occasionally exhibit rapid variability modulated by geomagnetic disturbances.

Observations since the early space age have recorded transient enhancements in outer zone flux associated with the spontaneous injection of SEPs, occurring more frequently during periods of maximum sunspot number (Lorentzen et al., 2002; Sawyer & Vette, 1976; Selesnick et al., 2010). Understanding this dynamic behavior has become especially important in light of the radiation risks such enhancements pose to orbiting spacecraft. Detailed equatorial measurements from the Combined Release and Radiation Effects Satellite (CRRES) highlighted the risk by showing that long-lived enhancements can form on rapid (minute) timescales, coinciding with the arrival of a storm sudden commencement. A particularly dramatic example was observed following the arrival of a large interplanetary shock on 24 March 1991, resulting in a second >20-MeV proton belt at $L \sim 2.5$ lasting for hundreds of days (Blake et al., 1992; Mullen et al., 1991).

Simulations by Kress et al. (2004) and Kress et al. (2005) have shown how the arrival of a storm sudden commencement allows SEPs at tens of megaelectron volts to penetrate the inner magnetosphere through the front-side magnetopause. Attenuation of incoming particle trajectories due to the geomagnetic field prevents access to certain altitude-latitude combinations as a function of particle rigidity, an effect known as geomagnetic cutoff. This effect is temporarily suppressed during disturbed times, allowing SEPs to penetrate down to $L \sim 3$ via low-latitude entry. The subsequent restoration of geomagnetic cutoff (within timescales comparable to one drift orbit) then prevents particles from leaving. Previous studies attribute further inward transport during the March 1991 event to the coherent acceleration of trapped SEPs by an electric field pulse, induced by the shock's compression of the magnetosphere (Hudson et al., 1995; Li et al., 1993). Simulations showed that megaelectron volt particles drifting in time with the azimuthal pulse experienced rapid inward transport by approximately 1–2 R_e, forming the observed new belt on a timescale of minutes (Hudson et al., 1997). Both rapid and diffusive inward transport conserves the first and second adiabatic invariants while violating the third, leading to betatron acceleration and an increase in pitch angle from the increasing ratio of perpendicular to parallel energy. Rapid SEP injections may therefore be associated with significant energization and may not have clear signatures at high latitude.

The formation of trapped enhancements at $L > 2$ has also been observed over approximately day timescales, with a suggested mechanism being enhanced radial diffusion caused by a drift-resonant interaction with magnetosonic ultralow frequency (ULF) waves (Lorentzen et al., 2002; Selesnick et al., 2010). For the electron belts, this is believed to explain increases in trapped flux correlating to fluctuations in solar wind dynamic pressure, a source of ULF wave power (see Takahashi & Ukhorskiy, 2007). Kovtyukh (2016) derives proton diffusion coefficients from observations of flux and energy spectra near 1 MeV during times of $Kp \leq 2$, showing a dependence on drift frequency in the ULF Pc6 range. Li et al. (2016) demonstrate losses in ~100-keV protons near geostationary orbit (GEO) coinciding with observed local enhancements in ULF wave power. However, the diffusion of protons during strong disturbances has yet to be fully explored.

During a geomagnetic storm, buildup of the ring current can cause outward motion of drift orbits associated with conservation of the third invariant, in addition to field line curvature scattering due to breakdown of adiabatic motion along stretch field lines (Anderson et al., 1997). Engel et al. (2015, 2016) show that modeling these two effects can account for losses reaching $L \sim 2.5$ that were observed during two large storms. The outer boundary of trapped flux, controlled by these losses, can therefore move to lower L shell over several hours corresponding to buildup of the *Dst* index. Observations show the time taken for the outer boundary to recover is hundreds of days due to outward radial diffusion (Selesnick et al., 2010). Some trapped enhancements, particularly at high L, may therefore be short-lived because of subsequent variability.

The risk posed to spacecraft by enhancements in trapped proton flux is particularly significant in the context of solar cell degradation. Damage accumulates via collisional atomic displacements, referred to as nonionizing dose (Anspaugh, 1996), leading to a drop in performance and potential shortening of mission lifetime. A relatively new type of mission exposed to this effect is electric orbit raising (EOR), whereby satellites intended for GEO are raised slowly from their initial transfer orbit using all-electric propulsion. This technique was first applied to commercial GEO satellites in 2015 (see review by Lev et al., 2019) and enables lower-cost access to space by replacing chemical propellant and reducing wet mass. However, the raising process takes ~200 days, in comparison to just a few days for chemical propulsion (Horne & Pitchford, 2015). During this time, performing multiple passes through the Van Allen belts has been shown to significantly increase nonionizing radiation dose from trapped protons (Messenger et al., 2014).

Radiation belt models based on previously collected data are used by mission designers to prescribe suitable spacecraft shielding. In the case of the National Aeronautics and Space Administration AE-8 and AP-8 models (Vette, 1991), modeled flux is based on mission-averaged conditions with flux variation attributed to solar cycle; results do not take into account dynamic changes (Evans, 1996). The AE-9 and AP-9 models (Ginet et al., 2013) have been developed by incorporating more recent observational data and allow the user to address the problem of variability by selecting a confidence level that the flux will not exceed a given value. For different confidence levels, spatial variations in flux can be estimated based on templates of previously observed or modeled states of the radiation belts (Ginet et al., 2013).

The Tacsat-4 Solar Cell Experiment, put into highly elliptical orbit (700 × 12,050 km at 63.4° inclination), provided results used to study the predictiveness of various models. Jenkins et al. (2014) compare remaining solar cell output power (vs. beginning of life) after 2 years in orbit to model predictions, showing mea-
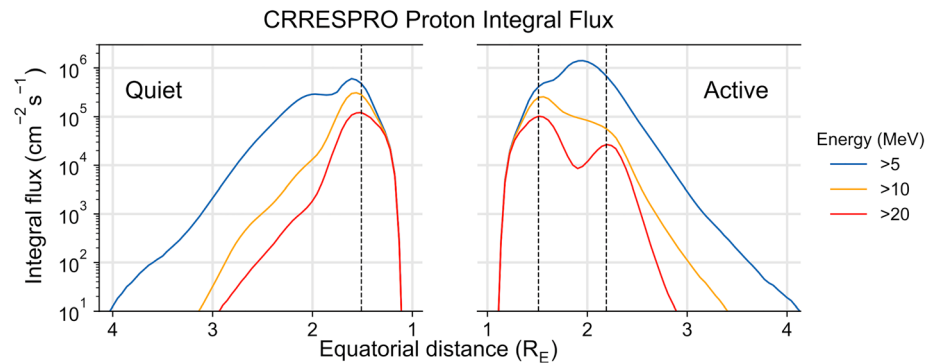
Figure 1. Proton integral flux on the geographic equator according to CRRESPRO Quiet (left panel) and Active (right panel). Integral flux is shown for >5 MeV (blue), >10 MeV (yellow), and >20 MeV (red). Vertical dashed lines represent the peaks of >20-MeV flux, showing two peaks in active conditions but only one peak in quiet conditions.

sured values >10% lower than predicted by AE-8 and AP-8, and ∼20% lower than predicted by AE-9 and AP-9 Mean. These results demonstrate the potential for radiation belt models to underpredict degradation when protons are the dominant contributor and have been used to update AP-9 in version 1.20 (Johnston et al., 2015).

In this work, we address the risk to EOR missions posed by dynamic enhancements in proton flux. These enhancements, associated with SEP trapping, can last for months before protons are released by a storm, and the effects are difficult to capture using design models. We achieve this aim by calculating nonionizing dose and associated solar cell degradation through time along three previously used EOR trajectories. Calculations are repeated for a quiet and active proton environment based on the March 1991 event to investigate the impact of a worst-case enhancement. The thickness of coverglass applied on top of the solar cell is also varied to investigate the impact of shielding. The impact of variations in environment, trajectory, and shielding on the dose accrued during EOR is discussed in light of these results. Finally, several key conclusions are drawn, summarizing the impact of proton belt enhancements in different circumstances of EOR and demonstrating ways it may be possible to mitigate degradation during future missions.

2. Modeling an Enhanced Environment

The 24 March 1991 storm observed by CRRES is one of the largest SEP trapping events for which equatorial observations of protons are available. CRRES's onboard Proton Telescope and High-Energy Electron Fluxmeter measured 1- to 100-MeV protons and 1- to 10-MeV electrons throughout its elliptical orbit (350 × 33,000 km) at 18° inclination. Proton Telescope data have previously been used to construct the time-averaged CRRESPRO proton belt model (Gussenhoven et al., 1993; Meffert & Gussenhoven, 1994), which includes Quiet and Active versions corresponding to conditions averaged over ∼200 days before and after the March 1991 storm. The difference between Quiet and Active versions therefore gives an example of the variation in trapped proton flux associated with a large enhancement.

In order to assess the impacts of an enhanced proton belt on solar array degradation, we have used these two models to compare degradation in a quiet environment (specified by CRRESPRO Quiet) with degradation in an active environment (specified by CRRESPRO Active). The choice of CRRESPRO was motivated by the goal of highlighting potential variability in solar cell degradation during EOR between two observed environments, rather than to provide the most realistic estimate of degradation possible in one case or another. Both environments are shown in Figure 1 in terms of integral flux. Above 20 MeV (red curve in Figure 1), the active state exhibits a second peak at 2.2 R_e due to newly trapped SEPs. At lower energies above 5 MeV (blue curve), high integral flux ($\gtrsim 10^5$ cm$^{-2} \cdot$ s^{-1}) persists until $L \sim 2.5$ in both quiet and active states.

Trapped electrons also contribute toward solar cell damage (Hands et al., 2018). However, the electron model (CRRESELE; see Brautigam & Bell, 1995) corresponding to CRRESPRO does not include electrons at $L < 2.5$ due to potential contamination of the data. This excludes a potentially important region for EOR; therefore, we do not use CRRESELE to measure the electron contribution. In the interest of understanding the final electron contribution to nonionizing dose, we later compare proton and electron damage when proton and electron environments are specified at an equivalent level of activity, using the AP-8/AE-8 MAX and

Table 1
Summary of Electric Orbit Raising Trajectories Used

Satellite	Launch date (DD/MM/YYYY)	Launch site	Designation	EOR duration (days)
SES-15	18/05/2017	Guiana Space Centre (5.2°N)	EOR-1	185
ABS-2A	14/06/2016	Kennedy Space Center (28.6°N)	EOR-2	200
SES-14	25/01/2018	Guiana Space Centre (5.2°N)	EOR-3	188

Note. EOR = electric orbit raising.

AP-9/AE-9 statistical model pairs. This gives a sense of the extra contribution to nonionizing dose missing from the calculations that include only CRRESPRO.

3. Satellite Trajectories

The calculation of optimal trajectories for EOR/low-thrust transfers has been a topic of active research since the mid-1970s (Messenger et al., 2014). A particularly significant challenge for the optimization process is taking into account diminishing thrust due to power loss (addressed recently by Kluever & Messenger, 2019). To illustrate the range of approaches used so far, we consider three trajectories based on previous EOR missions to GEO. The missions represented are as follows: SES-15, launched on 18 May 2017 from Guiana Space Centre (5.2°N); ABS-2A, launched on 14 June 2016 from Kennedy Space Centre (28.6°N); and SES-14, launched on 25 January 2018 from Guiana Space Centre. These scenarios are hereby referred to as EOR-1, EOR-2, and EOR-3, respectively, and summarized in Table 1. A measure of the EOR duration (in terms of trajectory) has been specified for each mission in Table 1 (column 5), corresponding to the day on which each satellite's longitude stopped increasing, and the satellite became parked at GEO altitude.

Each trajectory has been extrapolated from two-line element (TLE) orbit data. The PyEphem library (Rhodes, 2011) was used to convert TLE data to position at a given time, using the most recently available TLE. The spacecraft position was extracted at regular intervals for 200 days, starting from the time of the first TLE available after launch. This encompassed the EOR period for all three trajectories. The time step used to sample position throughout the 200 days was chosen based on the satellite's instantaneous speed at each previous position, such that the spacecraft traversed ∼600 km or less between samples. As the spacecraft's velocity was higher at perigee than at apogee, this method was used to ensure a consistent spatial resolution.

The trajectories produced as a result of the above process are shown in Figure 2 on the *X-Y* geographic equatorial plane. The locations of the two peaks in >20-MeV proton integral flux from the active environment model (shown in Figure 1) are indicated by two solid black concentric circles to show the location of the proton belt. A key characteristic of each orbit shown by Figure 2 is the initial apogee of the satellite as it enters a geostationary transfer orbit (GTO) after launch. The EOR-2 scenario (second panel) has an apogee that extends well past GEO altitude, whereas the apogee of EOR-1 (first panel) remains well within. From higher apogee, it is theoretically possible to raise perigee by a higher amount for a maneuver exerting the same impulse, potentially enabling a faster rate of raising.

4. Calculating Nonionizing Dose and Degradation

To calculate proton nonionizing dose, the total fluence was first calculated along each trajectory with the CRRESPRO Quiet or Active model using the European Space Agency's Spenvis interface (Heynderickx et al., 2005). Nonionizing dose was then calculated in terms of the displacement damage dose, Dd, using the MC-SCREAM tool (Messenger et al., 2010). This parameter is derived according to the method developed by the U.S. Naval Research Laboratory (Messenger et al., 2001). The effect of shielding was taken into account by the integrated MULASSIS transport code (Lei et al., 2002).

To calculate total dose as a function of time in Spenvis, the total fluence spectrum was recalculated for every day of EOR by repeatedly uploading larger and larger fractions of the 200-day trajectory. The calculation of
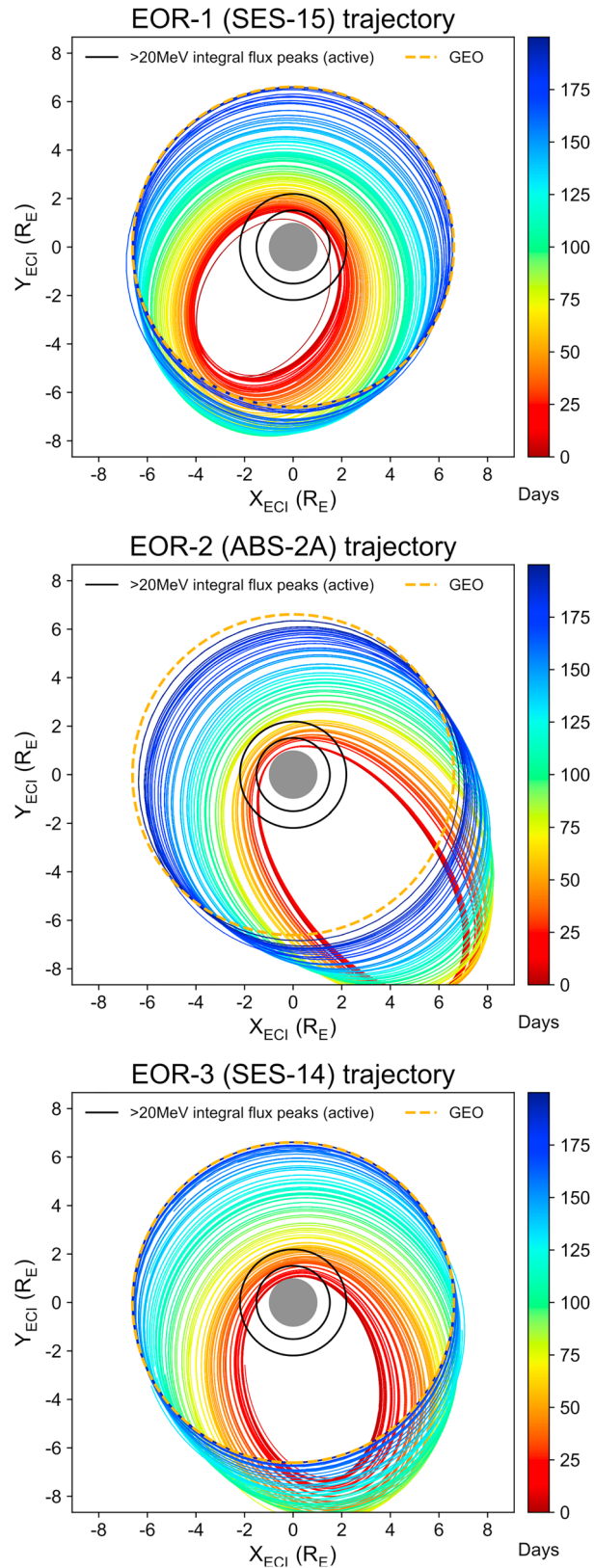
Figure 2. Trajectories of EOR-1 (SES-15), EOR-2 (ABS-2A), and EOR-3 (SES-14) over the first 200 mission days. The color coding indicates the number of days after launch. Peaks in >20-MeV integral flux during the active environment, shown in Figure 1, are indicated by black concentric rings for reference. GEO orbit is indicated by a yellow dashed line. EOR = electric orbit raising; GEO = geostationary orbit.
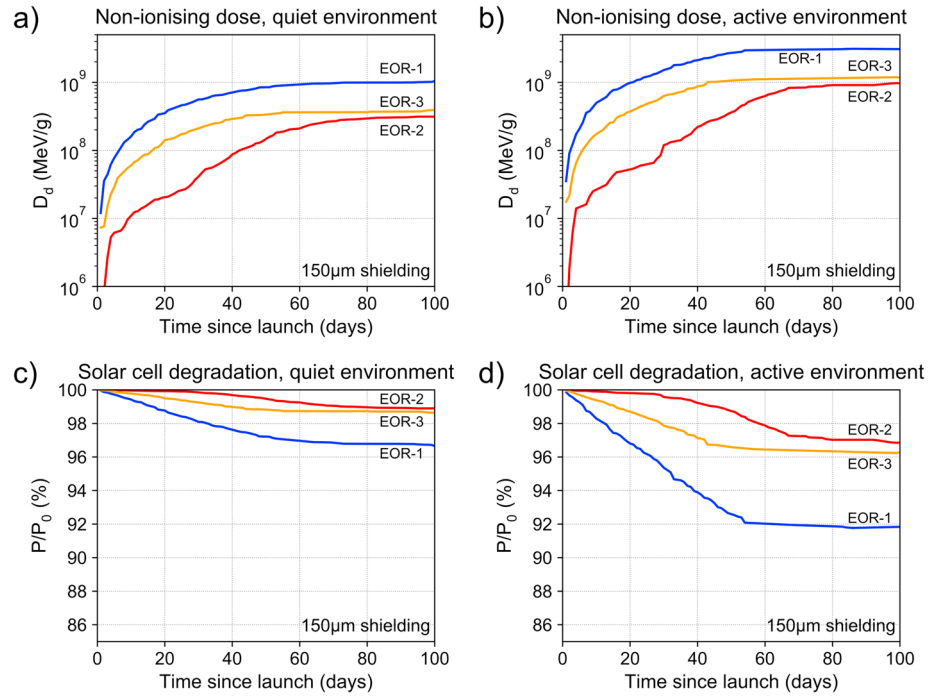
Figure 3. Displacement damage dose, Dd, (a, b) and remaining power, P/P0, (c, d) for three EOR trajectories for quiet (a, c) and active (b, d) conditions. Coverglass thickness is kept constant at 150 µm. EOR = electric orbit raising.

Dd was repeated for each daily total fluence spectrum using MC-SCREAM. We found this method resulted in lower error compared to summing Dd values obtained for incremental fluence spectrums.

For each trajectory and both environments, the calculation of dose through time was repeated for three thicknesses of solar cell coverglass: 100, 150, and 200 µm. This range includes levels of shielding previously used on satellites in highly exposed orbits such as Tacsat-4 (150 µm), as well as for solar panels qualified for GEO (typically 150 µm or less: Messenger et al., 2006; Spectrolab, 2010). Material density was kept constant with a typical value of 2.6 g/cm^3 (Qioptiq Space Technology, 2015). Calculations assumed that the back side of the solar cell was perfectly shielded. This may imply a small underestimate in dose depending on panel structure, which we estimate to be less than 5% at 200 days for any EOR scenario.

Each value of Dd was converted to the ratio of remaining solar cell output power relative to beginning of life: P/P0. This indicates the level of corresponding solar cell degradation and is a key indicator of remaining lifetime. Conversion from Dd to P/P0, for all calculations herein, was based on the characteristics of an Azur Space 3G30 triple junction solar cell, representative of current-generation technology. P/P0 is given by the characteristic equation:

$$\frac{P}{P_0} = 1 - C\log_{10}(1 + \frac{D_d}{D_x})$$

(1)

where C and D_x are experimentally determined fitting parameters. These are built into Spenvis for the 3G30 cell (0.306 and 3.63×10^9, respectively, for proton-equivalent Dd).

To investigate the balance between solar cell damage caused by protons and electrons at the end of EOR, the displacement damage dose from each species was calculated at day 200 for EOR-1, EOR-2, and EOR-3. A similar process was followed for each trajectory and coverglass thickness, but instead using the AP-8/AE-8 MAX and AP-9/AE-9 models to specify the same level of activity in proton and electron environments. AP-9/AE-9 models were run in percentile mode using the 95% setting. The effects of local time variation have not been included, having been found to cause a negligible difference for the orbits used.

5. Results

Figure 3 shows the displacement damage dose (Dd, panels a and b) and degradation in remaining power output (P/P0, panels c and d) as a function of time for all three EOR trajectories, for both quiet (a and c) and
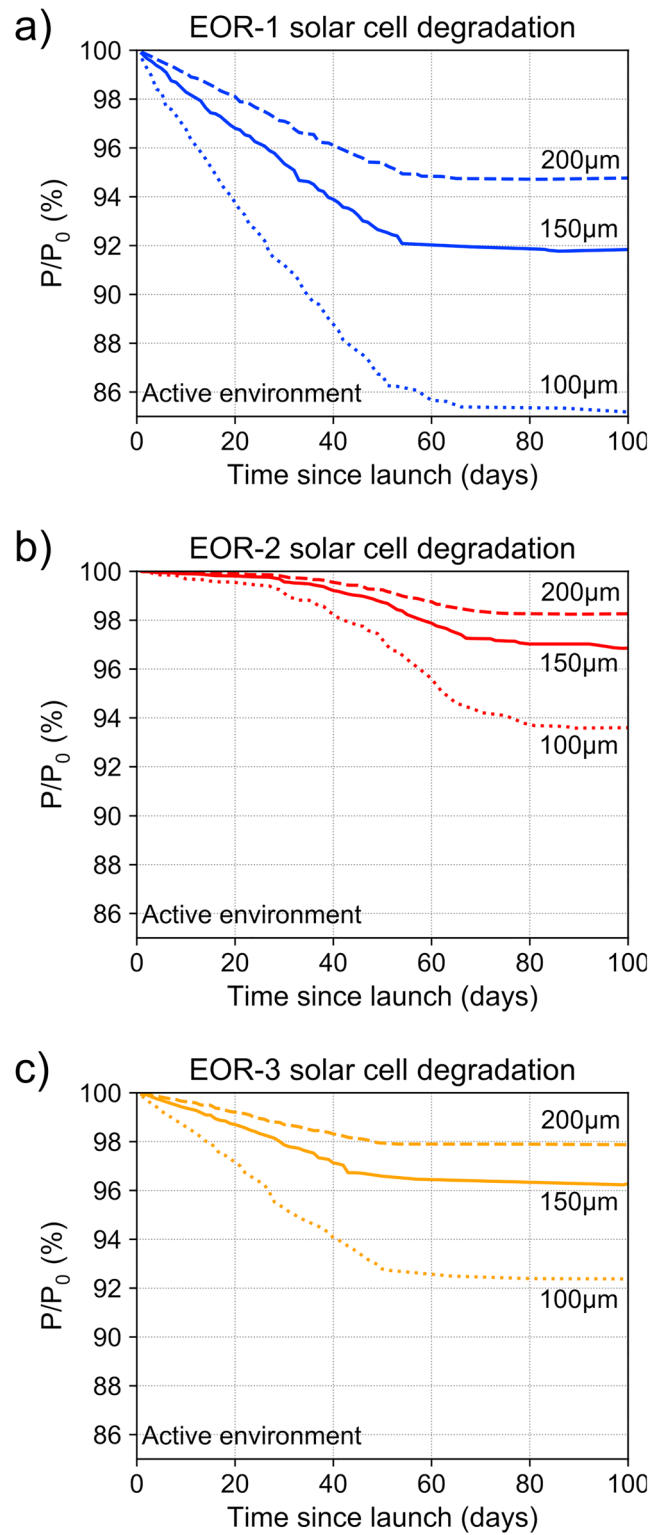
Figure 4. Solar cell degradation for all three EOR trajectories, calculated for different coverglass thicknesses in the active, poststorm environment. EOR = electric orbit raising.

Table 2
EOR Nonionizing Dose After 200 Days With AE-8/AP-8 MAX

Orbit	Shielding (μm)	Proton D_d (MeV/g)	Electron D_d (MeV/g)	Electron D_d contrib.	P/P_0 (excl. → inc. electrons)
	100	$1.05 \pm 0.04 \times 10^{10}$	$1.63 \pm 0.08 \times 10^{8}$	1.5%	81.9 → 81.8%
EOR-1	150	$4.59 \pm 0.21 \times 10^{9}$	$1.36 \pm 0.04 \times 10^{8}$	2.9%	89.1 → 88.9%
	200	$2.79 \pm 0.18 \times 10^{9}$	$1.28 \pm 0.04 \times 10^{8}$	4.4%	92.4 → 92.2%
	100	$4.55 \pm 0.34 \times 10^{9}$	$7.93 \pm 0.18 \times 10^{7}$	1.7%	89.2 → 89.1%
EOR-2	150	$1.67 \pm 0.12 \times 10^{9}$	$7.24 \pm 0.35 \times 10^{7}$	4.2%	95.0 → 94.8%
	200	$8.32 \pm 0.49 \times 10^{8}$	$6.05 \pm 0.15 \times 10^{7}$	6.8%	97.3 → 97.1%
	100	$4.98 \pm 0.26 \times 10^{9}$	$8.66 \pm 0.26 \times 10^{7}$	1.7%	88.5 → 88.4%
EOR-3	150	$1.91 \pm 0.19 \times 10^{9}$	$7.91 \pm 0.25 \times 10^{7}$	4.0%	94.4 → 94.2%
	200	$9.68 \pm 0.47 \times 10^{8}$	$7.67 \pm 0.36 \times 10^{7}$	7.3%	96.9 → 96.6%

Note. Errors shown relate to the calculations performed using the MC-SCREAM tool. EOR = electric orbit raising.

active (b and d) environments using 150-μm coverglass thickness. Only the first 100 days are shown, after which there was no significant increase in degradation until the end of EOR. This is primarily because the perigee of all three satellites had increased to a region of lower proton flux beyond 3 R_e. Figure 1 shows that an altitude of 3 R_e corresponds to a drop by over 2 orders of magnitude in >5-MeV integral flux compared to any value between 1.5 and 2 R_e, for both quiet and active environments.

For the quiet environment, Figure 3a shows that for EOR-2 (red curve) only minimal dose was accrued before day 30, after which dose rose steadily until around day 80. Figure 3c shows this resulted in a ~1% drop in P/P0 after 100 days. In contrast, for EOR-1 (blue curve), the dose accumulated for the most part between days 1–60, leading to a final power loss of ~3%.

For the active environment, Figure 3b shows the dose-time curves have a very similar shape to those for the quiet environment (panel a); dose increased primarily between days 30–80 for EOR-2 and days 1–60 for EOR-1/EOR-3. However, Figure 3d shows that the largest power drop in the active environment, occurring for EOR-1 (blue curve), was about 8%. This is somewhat larger than the 3% drop in power for quiet conditions (Figure 3c, blue curve). Both EOR-2 (red curve) and EOR-3 (amber curve) also show a larger drop in power during active conditions (3% and 4%, respectively, up from ~1%). Therefore the active environment resulted in 2% to 5% more degradation than the quiet environment.

To demonstrate the importance of solar cell coverglass shielding, the analysis of solar cell degradation in the active environment was repeated for three different thicknesses. Figure 4 shows P/P0 for all three EOR trajectories in an active environment, for coverglass thicknesses of 100, 150, and 200 μm. The results show that for EOR-1, as the coverglass thickness is increased from 100 μm to 150 μm to 200 μm, the amount of degradation is reduced, and the remaining power increases from 85% to 92% to 95%. A similar trend is shown for EOR-2 (94% to 97% to 98%) and EOR-3 (92% to 96% to 98%), although the effect is more pronounced for the EOR-1 trajectory with a higher exposure to nonionizing dose.

Figure 4 shows that when only 100-μm-thick coverglass is used, up to 15% degradation in power output can occur due to nonionizing dose from energetic protons during the first 100 days of electric orbit raising. However, the above results do not include the added contribution toward nonionizing dose from energetic electrons, or other effects such as coverglass darkening, and therefore are a lower limit on the power reduction.

To understand the extra impact from trapped electrons, the nonionizing dose caused by the presence of both species was calculated for the EOR-1, EOR-2, and EOR-3 scenarios using environments specified by the AE-8/AP-8 MAX models and again using the AE-9/AP-9 models at 95% percentile setting. Table 2 shows the nonionizing dose caused by protons and electrons separately after 200 days according to the AE-8/AP-8 MAX model. Table 3 shows the AE-9/AP-9 95% equivalent. The Dd caused by electrons is shown in terms of proton-equivalent dose so that it can be directly compared. In the fifth column of Tables 2 and 3, the

Table 3
EOR Nonionizing Dose After 200 Days With AE-9/AP-9 95%

Orbit	Shielding (μm)	Proton D_d (MeV/g)	Electron D_d (MeV/g)	Electron D_d contrib.	P/P$_0$ (excl. → inc. electrons)
	100	$1.32 \pm 0.04 \times 10^{10}$	$4.30 \pm 0.34 \times 10^{8}$	3.2%	79.6 → 79.3%
EOR-1	150	$5.38 \pm 0.30 \times 10^{9}$	$3.32 \pm 0.14 \times 10^{8}$	5.8%	87.9 → 87.4%
	200	$2.54 \pm 0.12 \times 10^{9}$	$3.02 \pm 0.12 \times 10^{8}$	10.6%	93.0 → 92.3%
	100	$5.65 \pm 0.27 \times 10^{9}$	$2.08 \pm 0.10 \times 10^{8}$	3.6%	87.5 → 87.2%
EOR-2	150	$1.69 \pm 0.08 \times 10^{9}$	$2.06 \pm 0.14 \times 10^{8}$	10.9%	94.9 → 94.4%
	200	$1.10 \pm 0.11 \times 10^{9}$	$1.66 \pm 0.09 \times 10^{8}$	13.1%	96.5 → 96.0%
	100	$1.05 \pm 0.07 \times 10^{10}$	$2.42 \pm 0.12 \times 10^{8}$	2.3%	81.9 → 81.7%
EOR-3	150	$3.07 \pm 0.14 \times 10^{9}$	$2.31 \pm 0.19 \times 10^{8}$	7.0%	91.9 → 91.4%
	200	$1.26 \pm 0.10 \times 10^{9}$	$1.81 \pm 0.06 \times 10^{8}$	12.6%	96.0 → 95.6%

Note. Errors shown relate to the calculations performed using the MC-SCREAM tool. EOR = electric orbit raising.

proportion of nonionizing dose attributed to electrons is shown as a percentage. The sixth column of Tables 2 and 3 shows P/P0 before and after taking the electron contribution into account.

Table 2 shows that according to AE-8/AP-8 MAX, electrons make up 1.5% to 7.3% of the total nonionizing dose depending on coverglass and trajectory. Table 3 shows that according to AE-9/AP-9 95%, the contribution is slightly higher, from 2.3% to 13.1%. Although electrons may therefore cause up to ~10% of the total displacement damage dose during EOR, the sixth column in Tables 2 and 3 show that the additional contribution causes a very small decrease in remaining power (less than 1%). This is because P/P0 falls off logarithmically with dose according to equation (1). Therefore, when the dose from protons is already high, extra exposure to electrons over the EOR duration causes a minor change.

Tables 2 and 3 also show that the relative contributions from protons and electrons to total dose during EOR depends on coverglass thickness, with the electron contribution (fifth column) becoming more significant as coverglass thickness increases. This is because nonionizing dose from protons decreases by 75% or more in each scenario when coverglass is increased from 100 to 200 μm (third column of Tables 2 and 3). In contrast, the decrease in nonionizing dose from electrons is about 30% at most (fourth column of Tables 2 and 3). A reason for this result is that increasing coverglass, in general, absorbs more of the low-energy portion of the incident spectrum. For electrons, unlike protons, it is the high-energy particles that do more damage per collision, and these fluxes are less affected (Messenger et al., 2001).

6. Discussion

6.1. The Influence of Orbit

The dose-time curves in Figures 3a and 3b show that after just 20 days, the solar arrays on EOR-1 had accrued a similar level of nonionizing dose to those on EOR-2 and EOR-3 after 100 days. It is important to understand why this occurred in order to be able to avoid such damage when possible. To investigate, we plot the total time spent in each 130-km-wide bin from $R = 1$ to $3R_E$, where R is the distance from the center of Earth to satellite. This bin sizing was found to be the most effective at highlighting certain features of each orbit discussed later. The time spent inside a bin after one pass is given by

$$\Delta t_b = \int_{R_{\text{enter}}}^{R_{\text{leave}}} \frac{\mathrm{d}t}{\mathrm{d}R}\, \mathrm{d}R, \tag{2}$$

where R_{enter} and R_{leave} are the distances at which the trajectory enters, leaves bin b, respectively. We sum each contribution given by equation (2) over every pass through the bin to find the total time spent by the satellite within 65 km of the bin center. Figure 5 shows the total time spent in each bin after the first 10, 20, 40, and 60 days (panels a to d) of EOR for each scenario (left ordinate). The >5-MeV integral flux given by the CRRESPRO quiet model is also shown for the same range of R (right ordinate).

Several peaks are apparent for each trajectory in Figure 5. These peaks occur due to the shape of the orbit: at perigee, dR/dt is small despite the satellite having higher overall speed, and fewer radial bins are crossed.
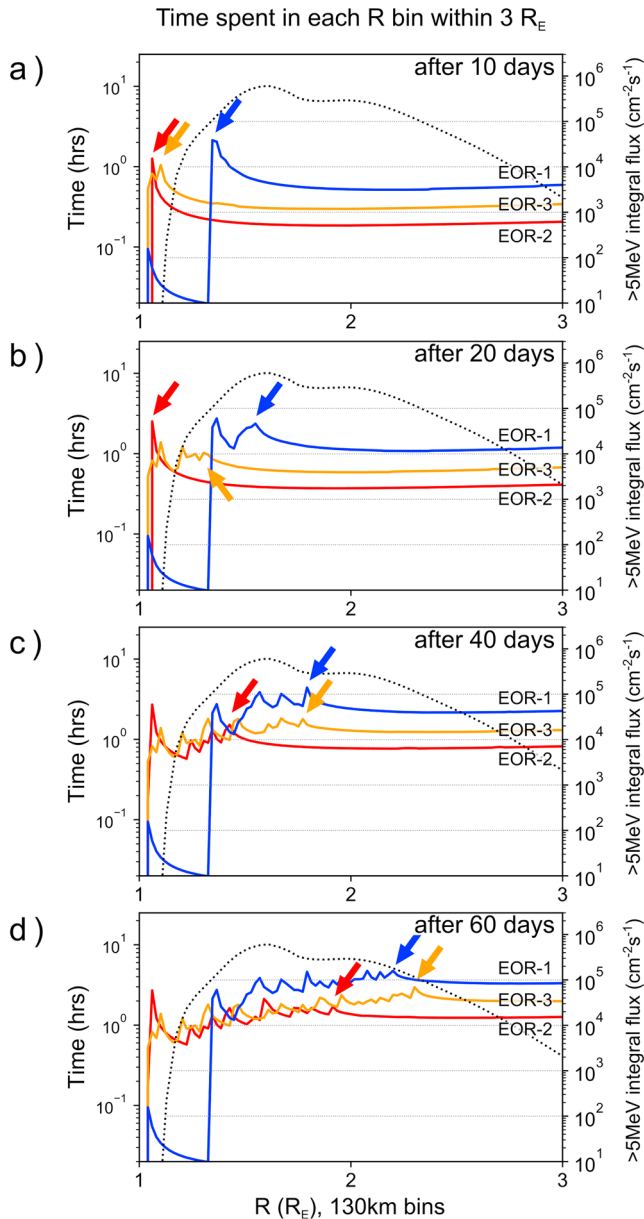
Figure 5. Total time spent in each 130-km-wide radius bin between $R_E = 1$ to 3 for each orbit, after (a) 10 days; (b) 20 days; (c) 40 days, and (d) 60 days. Colored arrows highlight the location of orbit perigee at each of these times for each satellite. The >5-MeV integral flux according to the quiet time CRRESPRO model is also included (right-hand scale). EOR = electric orbit raising.

Therefore, more time is accumulated in R bins near to orbit perigee. Conversely, away from perigee, the satellite passes quickly across different radii while changing altitude, spending less time in each bin. The peaks in Figure 5 therefore indicate the location of orbit perigee.

As orbit raising progresses for each satellite, the altitude of perigee is slowly increased by maneuvers. This is shown by the continuous addition of peaks in Figure 5 as the mission progresses from 10 to 60 days (panels a through d). The perigee at later times in each panel, indicated by the rightmost peak, is indicated by an arrow for each satellite.

Figure 5a shows that after only 10 days, the perigee of EOR-1 (blue curve) is raised up to $R \sim 1.3\,R_E$, marked by the blue arrow. As this is a region of high >5-MeV flux (dotted black line), EOR-1 begins accruing a large dose almost immediately. In contrast, the perigee of both EOR-2 (red curve) and EOR-3 (amber curve) remained low within this time period, indicated by the red and amber arrows.

Figure 5b shows that even after 20 days in orbit, the perigee of EOR-2 (red arrow) did not increase. This postlaunch period of a few weeks was instead used to reduce inclination, bringing the spacecraft into the equatorial plane. Therefore, EOR-2 stayed in its initial high-apogee GTO orbit, accruing very little dose because its perigee was beneath the region of high flux. Following this, EOR-2 began raising through the proton belt at a similar rate to EOR-3, indicated by the progression of the red arrow from day 20 to day 60 (panels b to d). This is faster than the rate at which EOR-1 perigee was raised, with EOR-3 perigee overtaking EOR-1 perigee by day 60 (panel d). Figure 5 thus shows that after 60 days, EOR-1 (blue curve) has spent more time within the region of high ($\gtrsim 10^4$ cm^{-2}·s^{-1}) >5-MeV flux, leading to a higher fluence and associated drop in P/P0. This is because it was placed into the high flux region early, then raised slowly. In contrast, EOR-2 (red curve) and EOR-3 (amber curve) were able to traverse the region of high >5-MeV trapped flux quickly. This demonstrates the utility of using an initial GTO with a high apogee that, in general, would allow faster raising of perigee. The small amount of dose EOR-2 accumulates within the first 20 days also shows the advantage of having a perigee beneath the proton belt when in GTO. This highlights the importance of modeling the location of innermost trapped flux accurately, shown by the steep gradient in the dotted line on the left of Figure 5, in order to understand exposure at low perigee.

6.2. Dependence of Dose on Shielding and Energy

For protons impacting solar cells without shielding, the highest damage per collision is caused by sub–megaelectron volt particles. This energy dependence is described both by experimentally determined relative damage coefficients and by calculated nonionizing energy loss coefficients (Messenger et al., 2001). Figure 4 shows that when coverglass thickness is increased, power loss is reduced. This demonstrates a change to the spectrum of particles after they have traversed the coverglass, caused by their initial energy being reduced. The three EOR scenarios together with the proton environment observed by CRRES provide an opportunity to test the dependence of nonionizing dose on the energy of incident flux before it impacts shielding.

To investigate, we calculated the average differential flux spectrum for EOR-2 after the first 100 days of EOR in the active environment. The spectrum was then modified by setting the flux to 0 above a "cutoff energy" and using MC-SCREAM to compute total dosage. Figure 6 shows that when the spectrum was set to 0 above 3 MeV for 100-µm coverglass, the dose was 0 (red curve). However, when the cutoff was increased to 7 MeV, the dose was the same as for the unmodified spectrum. Thus, for 100 µm, the important energy range is 3 to
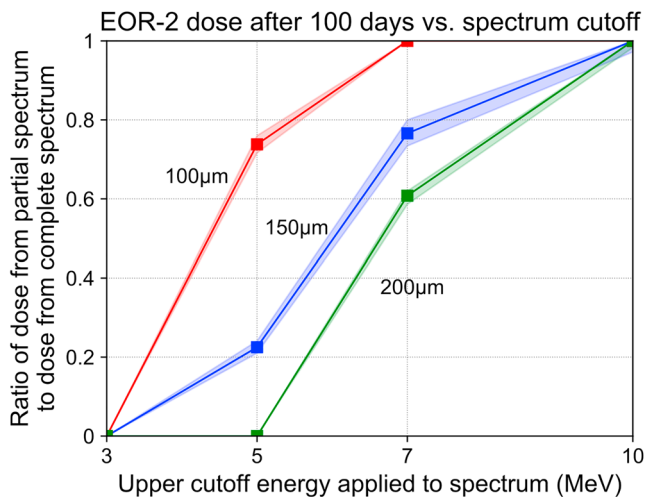
Figure 6. Ratio of total dosage calculated using a 100-day average differential flux spectrum for EOR-2, cut off after a certain energy, to the same calculation using the complete spectrum. The colored borders indicate error in the MULASSIS transport code calculation but do not take into account other limitations such as radiation belt model error or interpolation in energy. EOR = electric orbit raising.

7 MeV. As the coverglass thickness was increased, the important energy range was shifted up to between 3 and 10 MeV for 150 μm and 5 to 10 MeV for 200 μm. Therefore, for the range of shielding considered, only protons between 3 and 10 MeV make a significant contribution toward nonionizing dose. The dose imparted to shielded devices by different energies in an incident proton spectrum is addressed by Messenger et al. (1997), using a simulated solar proton event, and by Summers et al. (1997), for simulated inclined circular orbits. Results from these analyses show similar features, whereby a large fraction of total nonionizing dose can be attributed to a small energy range around 1 to 10 MeV.

A comparison between dose-time curves in the quiet and active environments (Figures 3a and 3b) shows a similar time period over which dose increases. Given that only 3- to 10-MeV flux contributes significantly, the reason for this similarity is explained by comparing quiet and active conditions at this energy. Figure 1 shows that high values of >5-MeV integral flux ($\gtrsim 10^5$ cm$^{-2}\cdot$s^{-1}) persist until $R \sim 2.5\,R_e$ in both quiet and active times. Therefore, fluxes near 3–10 MeV do not show a significant change in radial extent between active and quiet conditions, and degradation continues for roughly the same amount of time until the satellite reaches higher altitude. The addition of a >20-MeV flux peak within the slot region does not cause prolonged degradation in active times because the contribution from high energy toward nonionizing dose is low.

Figure 4 shows how power loss through time can be reduced with the application of thicker coverglass. An interesting result of increasing coverglass thickness is the shortening of the time window over which power loss occurs. For example, EOR-2 (panel b) stops accumulating dose after ~70 days for 200 μm compared with ~90 days for 100 μm, with a subtle but similar effect seen for EOR-1 and EOR-3. As the coverglass thickness is increased, the damaging part of the spectrum is shifted to higher energies within the 3- to 10-MeV range (Figure 6), but as Figure 1 shows, higher-energy fluxes tend to fall off more rapidly with radial distance. This reduces the time window during which the solar panel is subject to significant nonionizing dose.

The significance of 3- to 10-MeV environmental fluxes also highlights the importance of understanding the physical processes behind enhancements in this energy range. The radial transport of trapped particles to low L (in both a diffusive and shock-induced manner) is associated with significant energization. Therefore, SEPs contributing to the formation of $\lesssim$10-MeV enhancements may enter the magnetosphere at considerably lower energy. Particle tracing simulations by Richard et al. (2002) show that entry of SEPs to the magnetosphere near 1 MeV can be via the cusp or flank regions and is strongly influenced by interplanetary magnetic field orientation, whereas direct entry and trapping through the front-side magnetopause generally applies to SEPs at $\gtrsim$10 MeV. The various types of entry may therefore complicate modeling of source populations.

Although thicker coverglass is useful to reduce nonionizing dose, this is one area where various engineering and cost requirements may take priority. For example, there may also be a knock-on effect due to the increase in mass of thicker coverglass, such as the need to upgrade solar array drive mechanisms and structure. In this vein, it is useful to consider that increasing coverglass thickness tends to follow a law of diminishing returns, in terms of reducing total solar panel degradation during EOR, as demonstrated in Figure 4 for all three missions.

7. Summary and Conclusions

In this paper, we present an analysis of nonionizing dose from trapped protons accrued over 200 days during the course of EOR. Results show the variability caused by realistic changes to environment, trajectory, and coverglass thickness. Several key conclusions can be drawn from this work.

1. For a typical coverglass thickness of 150 μm, launching in an active environment can increase solar cell degradation due to trapped protons by 2% to 5% before start of service compared to a quiet environment depending on trajectory. These values are in terms of remaining power, normalized to beginning of life.

2. The crucial energy range for enhancements in proton flux is 3–10 MeV for solar cells with a level of shielding between 100 and 200 µm.

3. For a coverglass thickness of 150 µm, solar cell degradation in an active environment can vary by ∼5% for different EOR scenarios. In the EOR-1 scenario, solar cell degradation in an active environment can vary by ∼10% based on the choice of coverglass thickness between 100 and 200 µm. For EOR-2, this variation is around 5%.

4. In the worst case tested (active environment, 100-µm coverglass, EOR-1), degradation of up to 15% is possible within the EOR period, before taking into account other effects such as electron dose.

5. In addition to the degradation caused by trapped proton flux, evaluations of nonionizing dose at the end of the EOR period indicate an extra contribution from trapped electrons. This contribution is on the order of ∼10% or less in terms of the displacement damage dose. However, due to the dose already being high and because power decreases logarithmically with dose, adding this contribution has only a minor effect (less than 1%) on the remaining power predicted at the end of the raising period. This also casts estimates of further solar cell degradation due to trapped electrons at GEO in a new light, since operators will need to recalibrate P/P0 estimates based on dose accrued during EOR.

6. A higher initial orbit apogee generally implies that perigee can be raised faster during EOR, allowing the satellite to skip through the belt in fewer passes while also implying a higher velocity at perigee. These two factors mean less time is spent within the proton belt during raising from a high-apogee GTO. It is therefore recommended that EOR missions begin this way, such as in the case of EOR-2 (and EOR-3 to a lesser extent).

Several effects not taken into account in this analysis may reduce the transmission efficiency of solar cell coverglass, causing a further drop in performance. This can occur due to coverglass darkening from radiation damage, as well as the deposition of ions ejected from electric thrusters (Horne & Pitchford, 2015). Arc-induced contamination may also contribute toward solar cell power degradation throughout low Earth orbit, medium Earth orbit, and GEO environments depending on the grounding of conducting surfaces (Ferguson et al., 2016).

The importance of considering dynamic enhancements in trapped protons suggests a role for physics-based modeling to help assess radiation damage and address the increasing utilization of low and medium Earth orbits. However, more real-time information is required on the transient nature of the proton belt's outer region to understand these processes. In particular, the demonstrated importance of enhancements near 3–10 MeV near the equator at low L, which may not show signatures at high latitude due to transport energization, highlights the need for improved observational capability.

References

Albert, J. M., & Ginet, G. P. (1998). CRRES observations of radiation belt protons: 2. Time-dependent radial diffusion. *Journal of Geophysical Research*, *103*(A7), 14,865–14,877. https://doi.org/10.1029/98ja00290

Anderson, B. J., Decker, R. B., Paschalidis, N. P., & Sarris, T. (1997). Onset of nonadiabatic particle motion in the near-Earth magnetotail. *Journal of Geophysical Research*, *102*(A8), 17,553–17,569. https://doi.org/10.1029/97ja00798

Anspaugh, B. E. (1996). *GaAs solar cell radiation handbook*. Pasadena, CA: California Institute of Technology, JPL Publication.

Blake, J. B., Kolasinski, W. A., Fillius, R. W., & Mullen, E. G. (1992). Injection of electrons and protons with energies of tens of MeV into L < 3 on 24 March 1991. *Geophysical Research Letters*, *19*(8), 821–824. https://doi.org/10.1029/92gl00624

Brautigam, D. H., & Bell, J. T. (1995). CRRESELE documentation. https://doi.org/10.21236/ada301770

Engel, M. A., Kress, B. T., Hudson, M. K., & Selesnick, R. S. (2015). Simulations of inner radiation belt proton loss during geomagnetic storms. *Journal of Geophysical Research: Space Physics*, *120*, 9323–9333. https://doi.org/10.1002/2015ja021568

Engel, M. A., Kress, B. T., Hudson, M. K., & Selesnick, R. S. (2016). Comparison of Van Allen Probes radiation belt proton data with test particle simulation for the 17 March 2015 storm. *Journal of Geophysical Research: Space Physics*, *121*, 11,035–11,041. https://doi.org/10.1002/2016ja023333

Evans, H. (1996). The use of space radiation environment models for ESA mission evaluations. In W.Burke, & T.-D. Guyenne (Eds.), *Environment modeling for space-based applications* (Vol. 392, pp. 111). Noordwijk: (ESA SP-392). ESTEC.

Fälthammar, C. G. (1965). Effects of time-dependent electric fields on geomagnetically trapped radiation. *Journal of Geophysical Research*, *70*(11), 2503–2516. https://doi.org/10.1029/jz070i011p02503

Ferguson, D., Crabtree, P., White, S., & Vayner, B. (2016). Anomalous Global Positioning System power degradation from arc-induced contamination. *Journal of Spacecraft and Rockets*, *53*(3), 464–470. https://doi.org/10.2514/1.A33438

Ginet, G. P., O'Brien, T. P., Huston, S. L., Johnston, W. R., Guild, T. B., Friedel, R., & Su, Y. J. (2013). AE9, AP9 and SPM: New models for specifying the trapped energetic particle and space plasma environment, *The Van Allen Probes Mission* (pp. 579–615). Boston, MA: Springer US. https://doi.org/10.1007/978-1-4899-7433-4_18

Gussenhoven, M., Mullen, E., Violet, M., Hein, C., Bass, J., & Madden, D. (1993). CRRES high energy proton flux maps. *IEEE Transactions on Nuclear Science*, *40*(6), 1450–1457. https://doi.org/10.1109/23.273519

Hands, A. D. P., Ryden, K. A., Meredith, N. P., Glauert, S. A., & Horne, R. B. (2018). Radiation effects on satellites during extreme space weather events. *Space Weather*, *16*, 1216–1226. https://doi.org/10.1029/2018sw001913

Heynderickx, D., Quaghebeur, B., Wera, J., Daly, E., & Evans, H. (2005). ESA's Space Environment Information System (SPENVIS): A web-based tool for assessing radiation doses and effects in spacecraft systems. In *Space Nuclear Conference 2005, Proceedings of the embedded topical meeting, June 5-9, San Diego, California*, pp. 548–552.

Horne, R. B., & Pitchford, D. (2015). Space weather concerns for all-electric propulsion satellites. *Space Weather*, *13*, 430–433. https://doi.org/10.1002/2015sw001198

Hudson, M. K., Elkington, S. R., Lyon, J. G., Marchenko, V. A., Roth, I., Temerin, M., & Wygant, J. R. (1997). Simulations of radiation belt formation during storm sudden commencements. *Journal of Geophysical Research*, *102*(A7), 14,087–14,102. https://doi.org/10.1029/97ja03995

Hudson, M. K., Kotelnikov, A. D., Li, X., Roth, I., Temerin, M., Wygant, J., & Gussenhoven, M. S. (1995). Simulation of proton radiation belt formation during the March 24, 1991 SSC. *Geophysical Research Letters*, *22*(3), 291–294. https://doi.org/10.1029/95GL00009

Jenkins, P. P., Bentz, D. C., Barnds, J., Binz, C. R., Messenger, S. R., Warner, J. H., et al. (2014). TacSat-4 solar cell experiment: Two years in orbit. ESA Special Publication vol. 719.

Jentsch, V. (1981). On the role of external and internal source in generating energy and pitch angle distributions of inner-zone protons. *Journal of Geophysical Research*, *86*(A2), 701. https://doi.org/10.1029/ja086ia02p00701

Johnston, W. R., O'Brien, T. P., & Ginet, G. P. (2015). Release of AE9/AP9/SPM radiation belt and space plasma model version 1.20.002. *Space Weather*, *13*, 368–368. https://doi.org/10.1002/2015sw001212

Kluever, C. A., & Messenger, S. R. (2019). Solar-cell degradation model for trajectory optimization methods. *Journal of Spacecraft and Rockets*, *56*(3), 844–853. https://doi.org/10.2514/1.A34189

Kovtyukh, A. S. (2016). Deduction of the rates of radial diffusion of protons from the structure of the Earth's radiation belts. *Annales Geophysicae*, *34*(11), 1085–1098. https://doi.org/10.5194/angeo-34-1085-2016

Kress, B. T., Hudson, M. K., Perry, K. L., & Slocum, P. L. (2004). Dynamic modeling of geomagnetic cutoff for the 23–24 November 2001 solar energetic particle event. *Geophysical Research Letters*, *31*, L04808. https://doi.org/10.1029/2003GL018599

Kress, B. T., Hudson, M. K., & Slocum, P. L. (2005). Impulsive solar energetic ion trapping in the magnetosphere during geomagnetic storms. *Geophysical Research Letters*, *32*, L06108. https://doi.org/10.1029/2005GL022373

Lei, F., Truscott, R. R., Dyer, C. S., Quaghebeur, B., Heynderickx, D., Nieminen, R., & Daly, E. (2002). MULASSIS: A Geant4-based multilayered shielding simulation to. *IEEE Transactions on Nuclear Science*, *49*(6), 2788–2793. https://doi.org/10.1109/TNS.2002.805351

Lev, D., Myers, R. M., Lemmer, K. M., Kolbeck, J., Koizumi, H., & Polzin, K. (2019). The technological and commercial expansion of electric propulsion. *Acta Astronautica*, *159*, 213–227. https://doi.org/10.1016/j.actaastro.2019.03.058

Li, X., Roth, I., Temerin, M., Wygant, J. R., Hudson, M. K., & Blake, J. B. (1993). Simulation of the prompt energization and transport of radiation belt particles during the March 24, 1991 SSC. *Geophysical Research Letters*, *20*(22), 2423–2426. https://doi.org/10.1029/93GL02701

Li, L. Y., Yu, J., Cao, J. B., Wang, Z. Q., Yu, Y. Q., Reeves, G. D., & Li, X. (2016). Effects of ULF waves on local and global energetic particles: Particle energy and species dependences. *Journal of Geophysical Research: Space Physics*, *121*, 11,007–11,020. https://doi.org/10.1002/2016JA023149

Lorentzen, K. R., Mazur, J. E., Looper, M. D., Fennell, J. F., & Blake, J. B. (2002). Multisatellite observations of MeV ion injections during storms. *Journal of Geophysical Research*, *107*(A9), 1231. https://doi.org/10.1029/2001JA000276

Mazur, J. E., Blake, J. B., Slocum, P. L., Hudson, M. K., & Mason, G. M. (2013). The creation of new ion radiation belts associated with solar energetic particle events and interplanetary shocks. In N. Gopalswamy, R. Mewaldt, & J. Torsti (Eds.), *Solar eruptions and energetic particles* (Vol. 165, pp. 345–352). Washington, DC: American Geophysical Union (AGU). https://doi.org/10.1029/165GM32

Meffert, J. D., & Gussenhoven, M. (1994). CRRESPRO documentation. PHILLIPS LAB HANSCOM AFB MA.

Messenger, S. R., Burke, E. A., Walters, R. J., Warner, J. H., Summers, G. P., & Morton, T. L. (2006). Effect of omnidirectional proton irradiation on shielded solar cells. *IEEE transactions on nuclear science*, *53*(6), 3771–3778.

Messenger, S. R., Jackson, E. M., Warner, J. H., & Walters, R. J. (2010). Scream: A new code for solar cell degradation prediction using the displacement damage dose approach. In *2010 35th IEEE Photovoltaic Specialists Conference*, pp. 001106–001111. https://doi.org/10.1109/PVSC.2010.5614713

Messenger, S. R., Summers, G. P., Burke, E. A., Walters, R. J., & Xapsos, M. A. (2001). Modeling solar cell degradation in space: A comparison of the NRL displacement damage dose and the JPL equivalent fluence approaches. *Progress in Photovoltaics: Research and Applications*, *9*(2), 103–121. https://doi.org/10.1002/pip.357

Messenger, S. R., Wong, F., Hoang, B., Cress, C. D., Walters, R. J., Kluever, C. A., & Jones, G. (2014). Low-Thrust Geostationary Transfer Orbit (LT2GEO) radiation environment and associated solar array degradation modeling and ground testing. *IEEE Transactions on Nuclear Science*, *61*(6), 3348–3355. https://doi.org/10.1109/TNS.2014.2364894

Messenger, S. R., Xapsos, M. A., Burke, E. A., Walters, R. J., & Summers, G. P. (1997). Proton displacement damage and ionizing dose for shielded devices in space. *IEEE Transactions on Nuclear Science*, *44*(6), 2169–2173. https://doi.org/10.1109/23.659032

Mullen, E. G., Gussenhoven, M. S., Ray, K., & Violet, M. (1991). A double-peaked inner radiation belt: Cause and effect as seen on CRRES. *IEEE Transactions on Nuclear Science*, *38*(6), 1713–1718. https://doi.org/10.1109/23.124167

Parker, E. N. (1960). Geomagnetic fluctuations and the form of the outer zone of the Van Allen radiation belt. *Journal of Geophysical Research*, *65*(10), 3117–3130. https://doi.org/10.1029/JZ065i010p03117

Qioptiq Space Technology (2015). Solar Cell Coverglasses, http://www.qioptiq.com/download/QST_2015_03_Datasheet_CoverGlass, Accessed: 2019-01-25.

Richard, R. L., El-Alaoui, M., Ashour-Abdalla, M., & Walker, R. J. (2002). Interplanetary magnetic field control of the entry of solar energetic particles into the magnetosphere. *Journal of Geophysical Research*, *107*(A8), 1184. https://doi.org/10.1029/2001JA000099

Sawyer, D. M., & Vette, J. I. (1976). AP-8 trapped proton environment for solar maximum and solar minimum (*NASA-TM-X-72605*): NASA Goddard Space Flight Center.

Selesnick, R. S., Baker, D. N., Jaynes, A. N., Li, X., Kanekal, S. G., Hudson, M. K., & Kress, B. T. (2014). Observations of the inner radiation belt: CRAND and trapped solar protons. *Journal of Geophysical Research: Space Physics*, *119*, 6541–6552. https://doi.org/10.1002/2014JA020188

Selesnick, R. S., Baker, D. N., Jaynes, A. N., Li, X., Kanekal, S. G., Hudson, M. K., & Kress, B. T. (2016). Inward diffusion and loss of radiation belt protons. *Journal of Geophysical Research: Space Physics*, *121*, 1969–1978. https://doi.org/10.1002/2015JA022154

Selesnick, R. S., Hudson, M. K., & Kress, B. T. (2010). Injection and loss of inner radiation belt protons during solar proton events and magnetic storms. *Journal of Geophysical Research*, *115*, A08211. https://doi.org/10.1029/2010JA015247

Selesnick, R. S., Looper, M. D., & Mewaldt, R. A. (2007). A theoretical model of the inner proton radiation belt. *Space Weather*, *5*, S04003. https://doi.org/10.1029/2006SW000275

Spectrolab (2010). Space Solar Panels, https://www.spectrolab.com/DataSheets/Panel/panels.pdf, Accessed: 2019-01-25.

Spjeldvik, W. N. (2000). Transient effects of solar energetic particle flux enhancements on the inner magnetosphere of the Earth. *Advances in Space Research*, *25*, 2307–2310. https://doi.org/10.1016/S0273-1177(99)00513-X

Summers, G. P., Messenger, S. R., Burke, E. A., Xapsos, M. A., & Walters, R. J. (1997). Low energy proton-induced displacement damage in shielded GaAs solar cells in space. *Applied Physics Letters*, *71*(6), 832–834. https://doi.org/10.1063/1.119660

Takahashi, K., & Ukhorskiy, A. Y. (2007). Solar wind control of Pc5 pulsation power at geosynchronous orbit. *Journal of Geophysical Research*, *112*, A11205. https://doi.org/10.1029/2007JA012483

Tverskoy, B. (1965). Transport and acceleration of charged particles in the Earth's magnetosphere. *Geomagnetism and Aeronomy*, *5*, 617.

Vette, J. I. (1991). The NASA/National Space Science Data Center trapped radiation environment model program (1964–1991). NSSDC/WDC-A-R&S 91-29.